

# Three-Dimensional Integration of Black Phosphorus Photodetector with Silicon Photonics and Nanoplasmonics

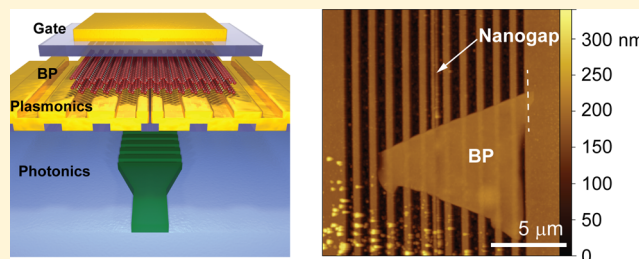
Che Chen, Nathan Youngblood,<sup>1</sup> Ruoming Peng, Daehan Yoo, Daniel A. Mohr, Timothy W. Johnson, Sang-Hyun Oh,<sup>1</sup> and Mo Li<sup>1\*</sup>

Department of Electrical and Computer Engineering, University of Minnesota, Minneapolis, Minnesota 55455, United States

## Supporting Information

**ABSTRACT:** We demonstrate the integration of a black phosphorus photodetector in a hybrid, three-dimensional architecture of silicon photonics and metallic nanoplasmonics structures. This integration approach combines the advantages of the low propagation loss of silicon waveguides, high-field confinement of a plasmonic nanogap, and the narrow bandgap of black phosphorus to achieve high responsivity for detection of telecom-band, near-infrared light. Benefiting from an ultrashort channel ( $\sim 60$  nm) and near-field enhancement enabled by the nanogap structure, the photodetector shows an intrinsic responsivity as high as 10 A/W afforded by internal gain mechanisms, and a 3 dB roll-off frequency of 150 MHz. This device demonstrates a promising approach for on-chip integration of three distinctive photonic systems, which, as a generic platform, may lead to future nanophotonic applications for biosensing, nonlinear optics, and optical signal processing.

**KEYWORDS:** Silicon photonics, plasmonics, black phosphorus, photodetector, nanogap, extraordinary optical transmission



Two-dimensional (2D) materials including graphene, transition metal dichalcogenides (TMDCs), black phosphorus (BP), and many others, offer novel optoelectronic properties that are very promising for a wide variety of photonic applications.<sup>1</sup> Optoelectronic devices based on these materials (e.g., photodetectors, optical modulators, light emitting diodes, and lasers) have been demonstrated with performances approaching, and sometimes rivaling, their commercial counterparts.<sup>2–4</sup> For these materials, many of their novel electrical and optical properties stem from their 2D nature, which provides out-of-plane quantum confinement and modifies their properties from those observed in bulk. However, the inherent thinness of mono- or few-layer materials also limits the optical interaction length and cross-section and, consequently, the total obtainable absorption, electro-optic effects, and nonlinearity. For example, while graphene boasts a remarkable universal absorption of 2.3% per layer over a very broad spectral band, this is often too small for many practical applications. To address this issue, various methods have been implemented to enhance light-matter interaction in 2D materials. Integrating 2D materials with planar photonic waveguides can extend the interaction length to the longitudinal dimension of the material, but at the expense of a larger footprint.<sup>5–9</sup> The increased footprint often has deleterious impacts on the total energy consumption and insertion loss of the final device. Alternatively, embedding 2D materials in optical cavities can resonantly enhance the light-matter interaction but only within the narrow band of the cavity resonance.<sup>10,11</sup> Nanoplasmonic structures can concentrate the optical field to subdiffraction-limit dimensions and dramatically enhance light-matter

interaction over a bandwidth much broader than dielectric optical resonators.<sup>12–19</sup> However, metal-based plasmonic devices have a high optical loss and thus are not suitable for long-distance propagation of optical signals.

From these considerations, it becomes clear that the optimal approach would be a hybrid of dielectric and plasmonic structures that can combine the advantages while avoiding the drawbacks of both platforms. There have been previous efforts to achieve such dielectric-plasmonic hybrid systems, such as hybrid waveguides to alleviate metal loss,<sup>20–24</sup> integrating plasmonic nanoantennas directly on silicon photonic waveguides,<sup>25,26</sup> and low-loss couplers between silicon and plasmonic waveguides.<sup>27,28</sup> In this Letter, we present a new hybrid architecture by integrating silicon photonics, plasmonic nanostructures, and a 2D material to construct a monolithically integrated photodetecting device. On this hybrid platform, infrared (IR) light is delivered via the silicon waveguide over a long distance, converted to surface plasmon polariton (SPP) waves and concentrated within a plasmonic nanogap on which the 2D material is integrated. For the 2D material, we use black phosphorus (BP), which is very attractive in optoelectronics for its direct and tunable bandgap ranging from  $\sim 2$  to 0.33 eV as the thickness increases from a monolayer to tens of nanometers.<sup>29,30</sup> BP is known to have good sensitivity in the near- and mid-IR regimes and various optoelectronic devices have been demonstrated such as a multispectral imager,<sup>31</sup>

**Received:** October 16, 2016

**Revised:** January 3, 2017

**Published:** January 10, 2017

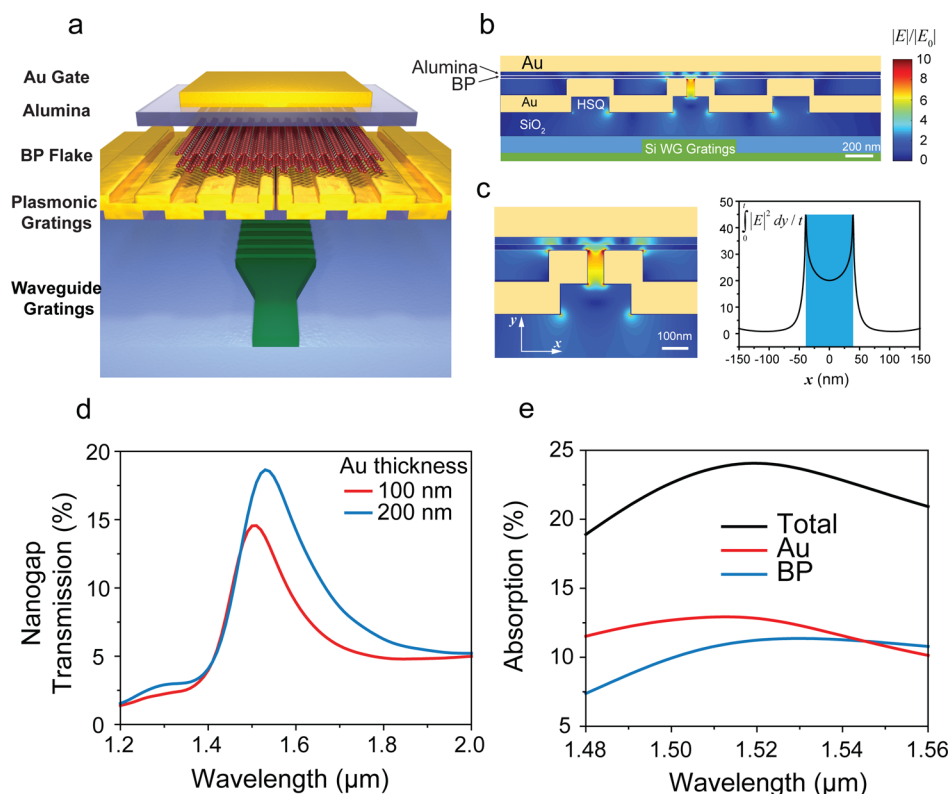


**Figure 1.** The 3D hybrid structure of silicon photonics, nanoplasmonics, and black phosphorus. (a) Artistic schematic of the integrated hybrid device with labels for different layers. (b) FDTD simulation of the optical mode coupling between the waveguide grating, metal grating, and the nanogap.  $|E|/|E_0|$  refers to the source amplitude in simulation. The BP layer is marked with the white box. (c) The simulation result highlights the significantly enhanced field amplitude distribution (left panel) and average optical intensity in the BP layer (right panel) in the BP–nanogap region. (d) Simulated transmission spectrum of the nanogap for 100 and 200 nm Au layer thickness, showing a resonance near the designed wavelength of 1.55  $\mu\text{m}$ . (e) The total absorption of the waveguide grating emission by the BP–nanogap structure found in FDTD with contributions from the BP (blue) and the metal (red).

polarization sensitive,<sup>32</sup> waveguide integrated near-IR,<sup>9</sup> and mid-IR photodetectors.<sup>33</sup> As we have discussed above, these devices suffer from either low responsivity when excited with normal incident light or a large device footprint when using a waveguide-integrated configuration.

The structure of the proposed hybrid system with a 3D architecture is illustrated conceptually in Figure 1a. It consists of three layers built on a standard silicon-on-insulator (SOI) platform: the bottom layer includes a silicon photonic waveguide with low propagation loss; the middle is the plasmonic layer comprising a metal grating and a nanogap; and the top layer consists of an exfoliated BP flake that is in direct contact with the metallic nanogap. A grating is patterned on the waveguide underneath the plasmonic structure to launch light out-of-plane through a spacing layer, thus coupling light from the waveguide to the nanogap. The output light from the waveguide grating (fundamental TE waveguide mode) is polarized in the  $x$ -direction, which is perpendicular to the nanogap direction. The metallic grating in the plasmonic structure converts the emission from the waveguide grating to an SPP wave and focuses it into the nanogap, where significantly enhanced optical intensity is obtained. It is notable that the metallic grating is fabricated by direct deposition of gold on prepatterned hydrogen silesquioxane (HSQ) resist, which provides a very smooth metal–dielectric interface with reduced scattering loss. Figure 1b shows a schematic cross-sectional view of this structure, overlaid with the electric field amplitude (normalized to the source amplitude  $|E|/|E_0|$ ) of the

optical mode simulated by the 2D finite-difference time-domain (FDTD) method. As visible in the field map, the extraordinary optical transmission (EOT) effect through the nanogap generates a highly concentrated optical field in the BP layer.<sup>34,35</sup> Figure 1c highlights the enhanced electric field amplitude inside the nanogap (left panel) and the profile of the averaged optical intensity in the BP layer (right panel), which exhibits an enhancement factor in the range of 20–45 relative to output intensity of waveguide grating.

To show the enhancement in optical transmission, Figure 1d plots the simulated transmission spectrum of the plasmonic nanostructure with a gap width of 60 nm. The simulation result indicates that when 100 nm (200 nm) thick gold layer is used in plasmonic gratings, 15% (18%) of the waveguide grating emission can be transmitted through the nanogap at the peak, corresponding to an EOT factor of 3.75 (4.50). Figure 1e plots the total optical absorption spectrum of the nanogap–BP hybrid and the respective contribution by the gold and the BP found in simulation. Although metal contributes more absorption (13% at peak) than BP, the light absorbed by BP is near 11% at peak (normalized to the power emitted from the waveguide gratings), which is significant given that the width of our aperture (60 nm) is much smaller as compared to other reported results.<sup>9,33</sup>

Our design is unique in that the metallic nanogap also serves as the source and drain contacts to the BP. Together with a metallic top gate, the nanogap and BP form a field effect transistor (FET) with an ultrashort channel of the width of the

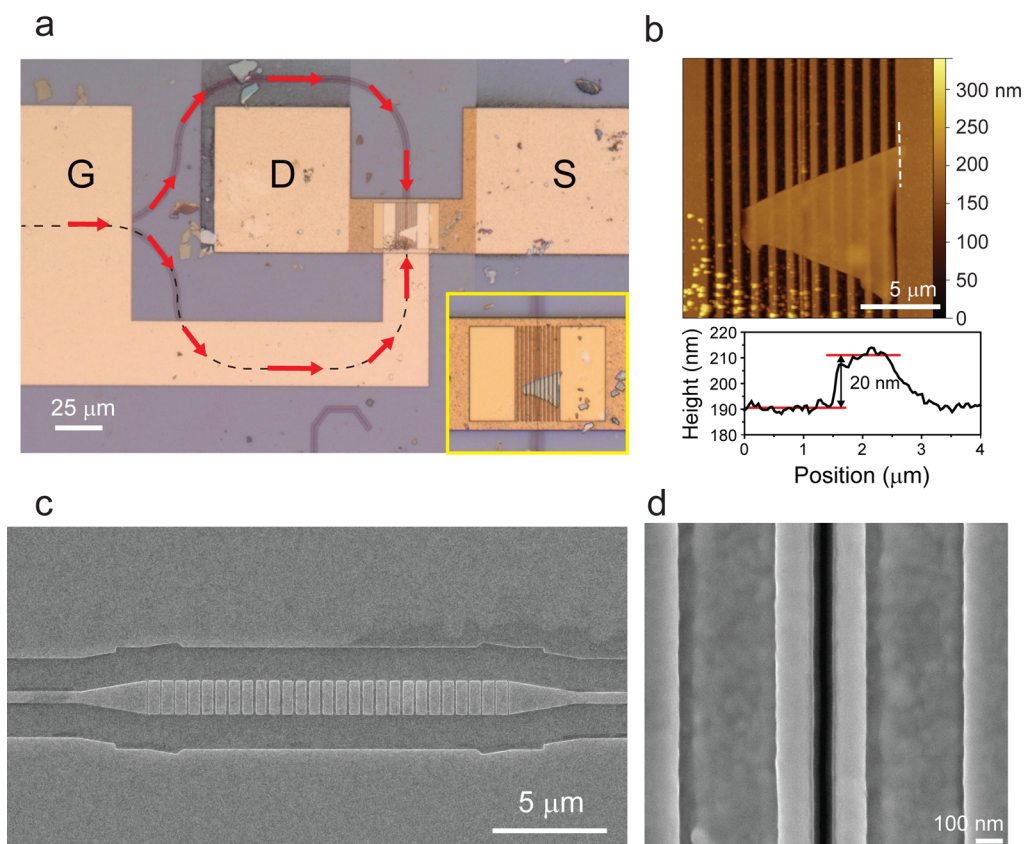


**Figure 2.** Microscope images of the device. (a) Optical microscope image of the completed device. The BP FET, using the metallic nanogap as the source and drain contacts, is integrated on top of the silicon waveguides (marked with black dashed lines). The red arrows indicate the direction of optical propagation. Inset: zoom-in microscope image of the BP–nanogap region (before patterning gate metal). (b) Atomic force microscope (AFM) image of the BP–nanogap region. The topographic profile (lower panel) along the dashed line shows that the BP flake is 20 nm thick. (c,d) Scanning electron microscope (SEM) images of the silicon waveguide grating (c) and the details of the nanogap (d), which shows a smooth and uniform gap with a width of 60 nm.

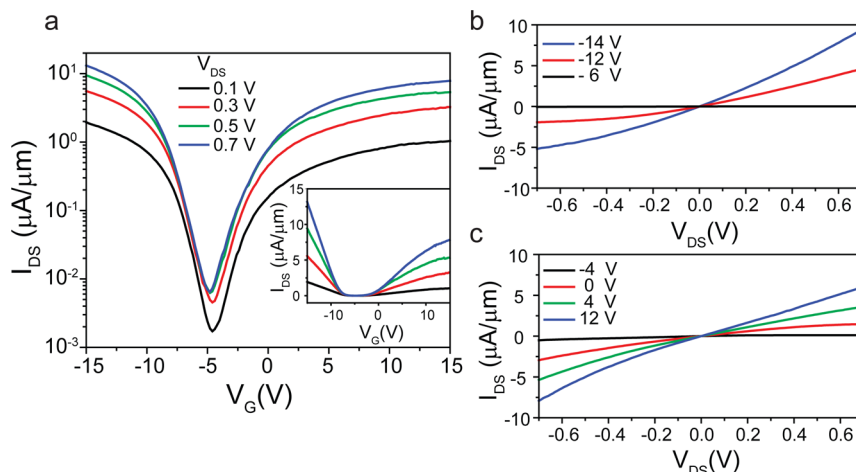


**Figure 3.** Electrical characterization of the BP FET. (a) Source-drain current,  $I_{DS}$ , plotted in log (main panel) and linear scales (inset), as the gate voltage  $V_G$  is swept while the bias voltage is fixed at various values. (b,c)  $I$ – $V$  characteristics of the device when the BP is gated to be p-doped (b) and n-doped (c), respectively.

nanogap. Additionally, the metallic top gate reflects the transmitted light back to the BP to further improve efficiency, which is confirmed through simulation (compare to Figure S2d). The combined benefits of low loss light delivery using a silicon waveguide, the concentration of light using plasmonics, and the ultrashort BP channel create an integrated BP photodetector with both high detection efficiency and speed.

The device fabrication process is described in detail in the [Methods section](#). Figure 2a shows an optical microscope image of the fabricated device. Thin BP flakes were exfoliated from crystals and transferred to the prefabricated substrates using a dry transfer method.<sup>36</sup> Figure 2b shows the atomic force microscope (AFM) image of the BP–nanogap region before the integration of the top gate. It shows that the BP flake, 20

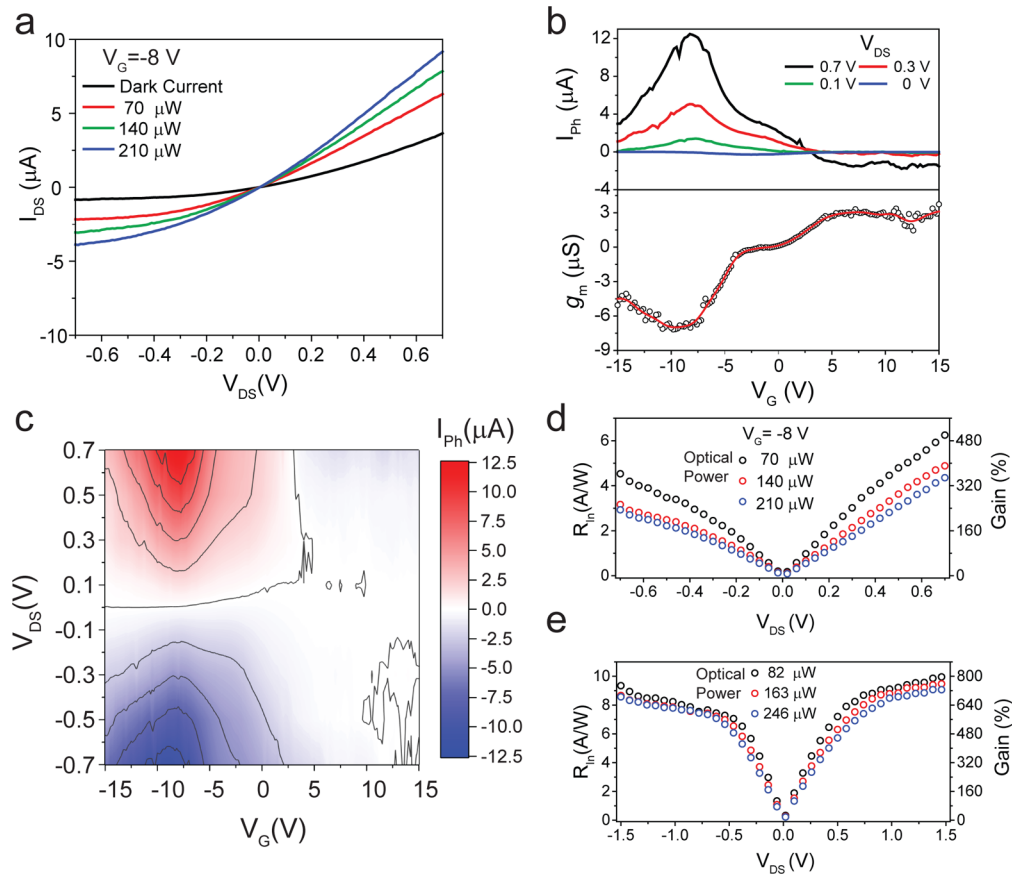


**Figure 4.** Photoresponse of the BP photodetector. (a) Source-drain current  $I_{DS}$  of the BP FET at a fixed gate voltage  $V_G$  ( $-8$  V) versus source-drain bias  $V_{DS}$  under varying optical power levels. The optical power levels refer to the emission at the silicon waveguide grating, determined by the calibration. (b) Photocurrent  $I_{ph}$  and transconductance  $g_m$  at optical power level of  $560 \mu\text{W}$  when the gate voltage is swept. The maximums of  $I_{ph}$  and  $g_m$  are coincident at the same gate voltage, suggesting the related gain mechanism. (c) Contour plot of photocurrent  $I_{ph}$  versus  $V_G$  and  $V_{DS}$ . A bolometric effect that generates negative photocurrent is weak in the device. (d) The intrinsic responsivity, referred to the absorbed optical power in BP, is as high as  $6.25 \text{ A/W}$ , corresponding to a photoconductive gain of 500%. (e) In another device without an integrated top gate, the highest responsivity is  $10 \text{ A/W}$  at  $1.5 \text{ V}$  source-drain bias and the corresponding photoconductive gain is 800%.

nm thick and  $10 \mu\text{m}$  wide across the nanogap, has been successfully transferred and integrated with the plasmonic nanostructures. The scanning electron microscope (SEM) image in Figure 2d shows that the nanogap has a very smooth profile with a width of  $60 \text{ nm}$  which was limited by the resolution of the focused ion beam (FIB) system we used. The SEM image of the silicon waveguide grating with a period of  $590 \text{ nm}$  and duty cycle of 78% is shown in Figure 2c.

The electrical characteristics of the device are shown in Figure 3. Figure 3a plots the source-drain current  $I_{DS}$  versus the gate voltage  $V_G$ . Our short-channel FET shows outstanding gate modulation of the channel current. Even at a moderately high bias ( $V_{DS}$ ) of  $0.7 \text{ V}$ , the on-off ratio is up to  $10^3$ , and the modulation depth is comparable to reported BP FETs with similar channel length.<sup>37</sup> Also, the device shows excellent ambipolar transport with channel conductance in the n-doped region being only a factor of 2 lower than the p-doped region in the measured range of  $V_G$ . The BP channel is tuned to be near intrinsic at a gate voltage of  $-4 \text{ V}$ , indicating the material is n-doped. In Figure 3b,c, the  $I$ - $V$  characteristics in different doping regimes are shown. In both p-type and n-type doping regions, the FET has linear  $I$ - $V$  characteristics, which implies comparable Schottky barriers for both holes and electrons. The slight asymmetry in  $I$ - $V$  curves at positive and negative bias can be attributed to bias modulating the barrier heights: in p-type

doped regime (negative gate bias), positive  $V_{DS}$  can further narrow the Schottky barrier and increase the conductance; on the contrary, in the n-type doped regime negative  $V_{DS}$  can narrow contact barrier and increase the conductance.<sup>38</sup>

Before showing the photodetection performance of the device, it is necessary to show how the light is routed to the BP photodetector in the hybrid system. Laser light is coupled from a fiber array into the waveguide through grating couplers with a typical coupling efficiency of  $\sim 20\%$ . The optical signal propagates to the waveguide grating and reemits upward. The waveguide grating (Figure 2c) is designed to have an efficiency of 48%, using adiabatically tapered duty cycles to mitigate back reflection. However, the measured efficiency is only 14%, which is attributed to fabrication imprecision and nonideality (see Supporting Information). This efficiency can be further improved by about a factor of 2 with the use of a back reflector.<sup>39</sup> With the assistance of the metal gratings on both sides of the nanogap, the emitted light excites SPP waves on the metallic nanostructure, which further propagates and funnels through the nanogap, leading to the EOT effect and significantly increased absorption in the BP layer (Figure 1d).

The device's photoresponse was measured when it operates in the photoconductive mode with an applied source-drain bias. Figure 4a shows the source-drain current  $I_{DS}$  at a fixed  $V_G$  of  $-8 \text{ V}$  at different optical power levels, marked in the legends as the

power emitted by the waveguide grating. It is clearly seen that photocurrent is generated in the BP channel with a magnitude that increases with the optical power. The photocurrent of the device is also highly dependent on the gate voltage, as shown in Figure 4b. The maximum photocurrent occurs near a gate bias of  $-8$  V, coincident with the peak of the FET transconductance  $g_m$ , as shown in the lower panel of Figure 4b, indicating an internal gain mechanism plays a role. Figure 4c shows a 2D contour plot of the photocurrent dependent on the gate and bias voltage. It is clear that the device shows very low negative photocurrent in the highly doped regions. Unlike the long channel devices,<sup>9,40</sup> the bolometric effect has a rather negligible contribution to the measured photocurrent. We attribute this to the large metal area in our device, which provides an efficient heat sink for the BP channel to dissipate heat quickly.

On the basis of the measurement results of photocurrent  $I_{ph}$ , the intrinsic responsivity  $R_{in} = I_{ph}/P_{abs}$ , where  $P_{abs}$  is absorbed optical power by the BP, and the photoconductive gain factor defined as  $G = R_{in}/(\eta e/h\nu)$ , where  $h\nu$  is photon energy,  $e$  is electron charge, and  $\eta$  is intrinsic quantum efficiency, are calculated and plotted in Figure 4d for different optical powers.  $P_{abs}$  is calculated based on the waveguide grating calibration and the simulation results in Figure 1. For example, when the estimated optical emission power from the BP covered gratings (BP covers 18% of the total grating area) is at  $12.6 \mu\text{W}$ , the external responsivity of the photodetector is  $214 \text{ mA/W}$ . Simulation (Figure 1b) suggests that the  $20 \text{ nm}$  BP layer absorbs 11% of the optical power emitted from the waveguide grating, and among this 31% is absorbed in the active BP area within the  $60 \text{ nm}$  wide channel, which generates the collected photocurrent. Therefore, the device achieves a remarkable intrinsic responsivity  $R_{in}$  of  $6.25 \text{ A/W}$  and a gain  $G$  of 500% at  $V_{DS} = 0.7 \text{ V}$ . Figure 4e shows the results of another device fabricated without the top gate, allowing application of higher bias without the concern of the large drain-gate field that may breakdown the BP. Its  $R_{in}$  is as high as  $10 \text{ A/W}$  at a bias voltage of  $1.5 \text{ V}$ . These values of responsivity are considerably higher than many previously reported results.<sup>9,31</sup> Also noticeable is that the responsivity reduces slightly with increasing optical power, which was previously observed in  $\text{MoS}_2$  photodetection measurements.<sup>41</sup> This slight decrease may be attributed to increased photocarrier recombination with increasing incident photons that generates a high concentration of excess carriers in the material, especially when considering the very high optical intensity in the nanogap.<sup>41</sup> We note that this saturation effect occurs at  $\mu\text{W}$  levels of optical power, significantly higher than that used in the devices reported previously.<sup>33,42,43</sup>

The larger than unity gain factor  $G$  indicates there are internal photocurrent gain mechanisms at play. Given the symmetric design of the device, the contribution of the photothermoelectric effect can be excluded.<sup>40</sup> The field effect mobility  $\mu_{FE}$  can be extracted from the transport results by using  $\mu_{FE} = g_m L / (WC_{ox} V_{DS})$ ,<sup>44</sup> where  $g_m$  is the transconductance,  $L = 60 \text{ nm}$  is the gate length,  $W = 4.5 \mu\text{m}$  (see Figure 2b) is the channel width, and  $C_{ox}$  is the gate oxide capacitance per unit area. The hole mobility is estimated to be  $0.96 \text{ cm}^2 \text{ V}^{-1} \text{ s}^{-1}$  in the linear regime (Figure 3a inset). The extracted mobility is likely to be very underestimated due to the high contact resistance in our device, and is consequently much lower than previously reported results.<sup>29,45</sup> We attribute the high contact resistance to directly transferring the BP flake onto the metal contacts. This process likely causes trapping of a high level of contaminants at the interface, as compared to forming

the contacts by directly depositing metal onto the BP. Using the extracted field mobility value, the carrier transit time in the BP channel can be calculated with  $\tau_{tr} = L^2 / (\mu_h V_{DS})$  to be  $53.6 \text{ ps}$ , whereas the carriers in bulk and at the surface of BP can be trapped with a longer lifetime. The coincidence of the maximum of the photocurrent and the maximum of  $g_m$  at the same gate voltage (Figure 4b) indicates that photogating effect related to charge trapping and the short transit time lead to a high photoconductive gain ( $G$ ) in our device.<sup>46</sup> In the photogating effect, one type of carrier is effectively trapped (by trap states or band bending) while the other type travels multiple times before they recombine. Moreover, the much higher hole mobility than the electron mobility in BP also facilitates the photoconductive gain.<sup>47</sup> The photoconductive gain (Figure 4d) of our device originates from the short BP channel length of only  $60 \text{ nm}$  enabled by the integration with the nanogap, and can be significantly increased if the carrier mobility can be improved and the contact resistance lowered.

It has been reported that the photogating effect in 2D materials due to photocarriers in midband traps states can dramatically enhance the optical responsivity, however, only at low frequency due to the very long trapping time.<sup>33,42,43</sup> We assessed the frequency response of the photodetector to an amplitude-modulated optical signal in the frequency range from  $2 \text{ kHz}$  to  $1.8 \text{ GHz}$ , as shown in Figure 5. A lock-in amplifier was

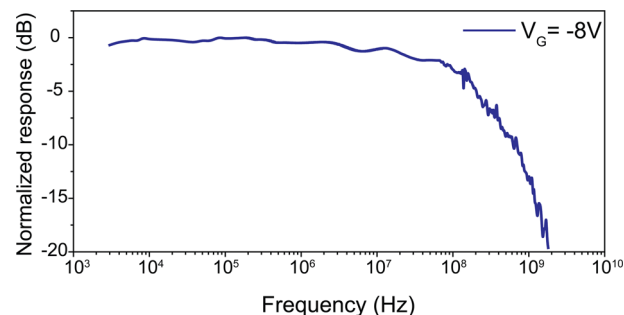


**Figure 5.** Frequency response of the BP photodetector to an amplitude-modulated optical signal. The 3 dB cutoff frequency is at  $150 \text{ MHz}$ , limited by the RC bandwidth of the device. The contact resistance of the device is the main factor that limits the high-speed performance of the device.

used from  $2$  to  $100 \text{ kHz}$  range and an RF network analyzer was used from  $100 \text{ kHz}$  to  $1.8 \text{ GHz}$  in the measurement. The photoresponse of the device shows a 3 dB roll-off frequency of  $150 \text{ MHz}$ . Although this cutoff frequency response is lower than that of previously demonstrated BP photodetectors,<sup>9</sup> it is considerably higher than that of devices dominated by the photogating effect,<sup>33</sup> and other reported results.<sup>31,33,48,49</sup> The current device's frequency response is limited by the RC time constant because, although the parasitic capacitance of the device is measured to be  $\sim 260 \text{ fF}$  at  $1 \text{ GHz}$ , the contact and channel resistance is very high.<sup>2</sup> Compared to our previous result,<sup>9</sup> the current device achieves very high responsivity due to a very short channel, but the frequency response is compromised by the high resistance. In the future, improving the contact to BP could be achieved by transferring the BP flakes in an ultraclean and inert environment to avoid contaminants and using a different adhesion metal layer between the BP and Au to lower the Schottky barrier.<sup>50</sup> Additionally, sandwiching BP between two layers of hexagonal boron nitride (h-BN) can not only improve the carrier mobility

in BP<sup>51</sup> but also allows for the fabrication of 1D edge contacts to BP to further reduce contact resistance.<sup>52</sup>

In conclusion, we have shown a BP infrared photodetector based on a 3D integration platform of silicon photonics and plasmonics. The photodetector's performance significantly benefits from silicon photonics' ability to deliver light over a long distance with a low loss and plasmonics' ability to concentrate light below the diffraction limit. Direct integration of BP on the plasmonic nanogap also naturally makes a short channel photodetector, enabling built-in photoconductive gain with a high detection bandwidth. Much higher photoconductive gain can be obtained when the nanogap width is further reduced to below 10 nm as has been achieved recently,<sup>53</sup> and the BP quality is improved to increase carrier mobility such that the carrier transport in the device may approach the ballistic regime. The optical loss at the waveguide grating and the plasmonic grating can be reduced by improving the waveguide grating design, adding a dielectric reflector under the waveguide grating, and more systematic optimization between the photonics and plasmonics layers. The results from the current device successfully demonstrate the feasibility and promise of such a hybrid approach of integrating 2D materials, plasmonics, and silicon photonics. Overall, this approach combines the best attributes of each technology while mitigating their respective disadvantages. Our demonstration of a photodetector with high responsivity and fast frequency response is only the first step. The approach can be adopted to make efficient optical modulators,<sup>54</sup> nonlinear optical devices,<sup>55</sup> and cointegration of 2D electronics with optoelectronics<sup>56</sup> with a broad range of potential applications including optical signal processing.<sup>57</sup>

**Methods. Device Fabrication.** The device was fabricated on a standard SOI wafer (220 nm silicon layer and 3  $\mu\text{m}$  buried oxide layer). The silicon photonic layer was fabricated with standard e-beam lithography (Vistec EBPG 5000+) and plasma dry etching processes and cladded with a 2  $\mu\text{m}$  silicon dioxide layer deposited by plasma-enhanced chemical vapor deposition. The plasmonic nanostructure was also fabricated with e-beam lithography by patterning the nanograting in a layer of hydrogen silsesquioxane (HSQ) resist and conformally depositing 3 nm of titanium and 120 nm of gold on top (Figure 1b). The nanogap was subsequently milled in the metal film with FIB. The BP flake was exfoliated and then transferred onto the plasmonic structure using a dry transfer method. Immediately after the transfer, 40 nm of aluminum oxide was deposited by atomic layer deposition. This served as the gate dielectric and also encapsulated the BP to prevent degradation. Finally, the top metal gate (3 nm Ti/100 nm Au) was patterned using e-beam lithography and metal deposition/lift-off.

**Photonic Layer Design.** The photonic layer was fabricated on an SOI wafer. There are two grating couplers patterned (Figure S3a): one is used to couple light into waveguide and the other one is used to monitor coupling efficiency. After the first Y-junction, half of the light is guided to the device area while the rest goes to the monitoring grating coupler. Before the light is guided to the waveguide grating, it is split into two parts evenly (by the second Y-junction) and the waveguide follows a race-track design. The symmetric design of the waveguide grating facilitates the emission of a more uniform output wavefront that can more efficiently excite the SPP wave on the metal grating and concentrate light in the nanogap (see Supporting Information).

**Photocurrent Measurement.** Photocurrent measurements were performed by scanning both gate and S/D (source/drain)

biases at a fixed laser wavelength, and measuring S/D currents. Two Keithley 2400 series source measure units (SMUs) were used in electrical measurements. Both SMUs were operated in source-voltage/measure-current mode. While one SMU applied the gate bias, the other applied the S/D bias and recorded current readings. By varying the optical power, the S/D current was measured, including the dark current. After extracting the dark current, the photocurrent was acquired for different optical power inputs at various bias conditions.

## ■ ASSOCIATED CONTENT

### 📄 Supporting Information

The Supporting Information is available free of charge on the ACS Publications website at DOI: 10.1021/acs.nanolett.6b04332.

Measurement setup; second device without top gate; silicon photonic layer design; FDTD simulation; plasmonic grating design; and additional figures (PDF)

## ■ AUTHOR INFORMATION

### Corresponding Author

\*E-mail: moli@umn.edu.

### ORCID

Nathan Youngblood: 0000-0003-2552-9376

Sang-Hyun Oh: 0000-0002-6992-5007

Mo Li: 0000-0002-5500-0900

### Notes

The authors declare no competing financial interest.

## ■ ACKNOWLEDGMENTS

This work was supported by the Air Force Office of Scientific Research (Award No. FA9550-14-1-0277; C.C., N.Y., R.P., M.L.) and the National Science Foundation (Award No. ECCS-1351002 for C.C., N.Y., R.P. M.L.; ECCS-1610333 for D.Y., D.A.M., T.W.J., S.-H.O.). D.A.M. also acknowledges support from the NIH Biotechnology Training Grant (T32 GM008347). Device fabrication was carried out at the University of Minnesota Nanofabrication Center, which receives partial support from the NSF through the National Nanotechnology Coordinated Infrastructure (NNCI) program. The authors also used resources at the Characterization Facility, which is a member of the NSF-funded Materials Research Facilities Network via the NSF MRSEC program.

## ■ REFERENCES

- (1) Xia, F.; Wang, H.; Xiao, D.; Dubey, M.; Ramasubramanian, A. *Nat. Photonics* **2014**, *8*, 899–907.
- (2) Xia, F.; Mueller, T.; Lin, Y.-M.; Valdes-Garcia, A.; Avouris, P. *Nat. Nanotechnol.* **2009**, *4*, 839–843.
- (3) Phare, C. T.; Daniel Lee, Y.-H.; Cardenas, J.; Lipson, M. *Nat. Photonics* **2015**, *9*, 511–514.
- (4) Huang, M.; Wang, M.; Chen, C.; Ma, Z.; Li, X.; Han, J.; Wu, Y. *Adv. Mater.* **2016**, *28*, 3481–3485.
- (5) Liu, M.; Yin, X.; Ulin-Avila, E.; Geng, B.; Zentgraf, T.; Ju, L.; Wang, F.; Zhang, X. *Nature* **2011**, *474*, 64–67.
- (6) Wang, X.; Cheng, Z.; Xu, K.; Tsang, H. K.; Xu, J.-B. *Nat. Photonics* **2013**, *7*, 888–891.
- (7) Gan, X.; Shiue, R.-J.; Gao, Y.; Meric, I.; Heinz, T. F.; Shepard, K.; Hone, J.; Assefa, S.; Englund, D. *Nat. Photonics* **2013**, *7*, 883–887.
- (8) Youngblood, N.; Anugrah, Y.; Ma, R.; Koester, S. J.; Li, M. *Nano Lett.* **2014**, *14*, 2741–2746.
- (9) Youngblood, N.; Chen, C.; Koester, S. J.; Li, M. *Nat. Photonics* **2015**, *9*, 249–252.

- (10) Furchi, M.; Urich, A.; Pospischil, A.; Lilley, G.; Unterrainer, K.; Detz, H.; Klang, P.; Andrews, A. M.; Schrenk, W.; Strasser, G.; Mueller, T. *Nano Lett.* **2012**, *12*, 2773–2777.
- (11) Engel, M.; Steiner, M.; Lombardo, A.; Ferrari, A. C.; Löhneysen, H. v.; Avouris, P.; Krupke, R. *Nat. Commun.* **2012**, *3*, 906.
- (12) Bozhevolnyi, S. I.; Volkov, V. S.; Devaux, E.; Laluet, J.-Y.; Ebbesen, T. W. *Nature* **2006**, *440*, 508–511.
- (13) Lal, S.; Link, S.; Halas, N. J. *Nat. Photonics* **2007**, *1*, 641–648.
- (14) Schuller, J. A.; Barnard, E. S.; Cai, W.; Jun, Y. C.; White, J. S.; Brongersma, M. L. *Nat. Mater.* **2010**, *9*, 193–204.
- (15) Ishi, T.; Fujikata, J.; Marita, K.; Baba, T.; Ohashi, K. *Japanese J. Appl. Physics, Part 2 Lett.* **2005**, *44*, L364–L366.
- (16) Akbari, A.; Tait, R. N.; Berini, P. *Opt. Express* **2010**, *18*, 8505.
- (17) Goykhman, I.; Desiatov, B.; Khurgin, J.; Shappir, J.; Levy, U. *Nano Lett.* **2011**, *11*, 2219–2224.
- (18) Goykhman, I.; Sassi, U.; Desiatov, B.; Mazurski, N.; Milana, S.; De Fazio, D.; Eiden, A.; Khurgin, J.; Shappir, J.; Levy, U.; Ferrari, A. C. *Nano Lett.* **2016**, *16*, 3005–3013.
- (19) Huang, K. C. Y.; Seo, M.-K.; Huo, Y.; Sarmiento, T.; Harris, J. S.; Brongersma, M. L. *Nat. Commun.* **2012**, *3*, 1005.
- (20) Wu, M.; Han, Z.; Van, V. *Opt. Express* **2010**, *18*, 11728–11736.
- (21) Delacour, C.; Blaize, S.; Grosse, P.; Fedeli, J. M.; Bruyant, A.; Salas-Montiel, R.; Lerondel, G.; Chelnokov, A. *Nano Lett.* **2010**, *10*, 2922–2926.
- (22) Briggs, R. M.; Grandidier, J.; Burgos, S. P.; Feigenbaum, E.; Atwater, H. A. *Nano Lett.* **2010**, *10*, 4851–4857.
- (23) Fedyanin, D. Y.; Yakubovsky, D. I.; Kirtaev, R. V.; Volkov, V. S. *Nano Lett.* **2016**, *16*, 362–366.
- (24) Nielsen, M. P.; Lafone, L.; Rakovich, A.; Sidiropoulos, T. P. H.; Rahmani, M.; Maier, S. A.; Oulton, R. F. *Nano Lett.* **2016**, *16*, 1410–1414.
- (25) Peyskens, F.; Dhakal, A.; Van Dorpe, P.; Le Thomas, N.; Baets, R. *ACS Photonics* **2016**, *3*, 102–108.
- (26) Luo, Y.; Chamanzar, M.; Apuzzo, A.; Salas-Montiel, R.; Nguyen, K. N.; Blaize, S.; Adibi, A. *Nano Lett.* **2015**, *15*, 849–856.
- (27) Choo, H.; Kim, M.-K.; Staffaroni, M.; Seok, T. J.; Bokor, J.; Cabrini, S.; Schuck, P. J.; Wu, M. C.; Yablonovitch, E. *Nat. Photonics* **2012**, *6*, 838–844.
- (28) Ono, M.; Taniyama, H.; Xu, H.; Tsunekawa, M.; Kuramochi, E.; Nozaki, K.; Notomi, M. *Optica* **2016**, *3*, 999.
- (29) Li, L.; Yu, Y.; Ye, G. J.; Ge, Q.; Ou, X.; Wu, H.; Feng, D.; Chen, X. H.; Zhang, Y. *Nat. Nanotechnol.* **2014**, *9*, 372–377.
- (30) Das, S.; Zhang, W.; Demarteau, M.; Hoffmann, A.; Dubey, M.; Roelofs, A. *Nano Lett.* **2014**, *14*, 5733–5739.
- (31) Engel, M.; Steiner, M.; Avouris, P. *Nano Lett.* **2014**, *14*, 6414–6417.
- (32) Yuan, H.; Liu, X.; Afshinmanesh, F.; Li, W.; Xu, G.; Sun, J.; Lian, B.; Curto, A. G.; Ye, G.; Hikita, Y.; Shen, Z.; Zhang, S.-C.; Chen, X.; Brongersma, M.; Hwang, H. Y.; Cui, Y. *Nat. Nanotechnol.* **2015**, *10*, 707–713.
- (33) Guo, Q.; Pospischil, A.; Bhuiyan, M.; Jiang, H.; Tian, H.; Farmer, D.; Deng, B.; Li, C.; Han, S.-J.; Wang, H.; Xia, Q.; Ma, T.-P.; Mueller, T.; Xia, F. *Nano Lett.* **2016**, *16*, 4648–4655.
- (34) García-Vidal, F. J.; Lezec, H. J.; Ebbesen, T. W.; Martín-Moreno, L. *Phys. Rev. Lett.* **2003**, *90*, 213901.
- (35) Garcia-Vidal, F. J.; Martín-Moreno, L.; Ebbesen, T. W.; Kuipers, L. *Rev. Mod. Phys.* **2010**, *82*, 729–787.
- (36) Castellanos-Gomez, A.; Buscema, M.; Molenaar, R.; Singh, V.; Janssen, L.; van der Zant, H. S. J.; Steele, G. A. *2D Mater.* **2014**, *1*, 011002.
- (37) Miao, J.; Zhang, S.; Cai, L.; Scherr, M.; Wang, C. *ACS Nano* **2015**, *9*, 9236–9243.
- (38) Penumatcha, A. V.; Salazar, R. B.; Appenzeller, J. *Nat. Commun.* **2015**, *6*, 8948.
- (39) Taillaert, D.; Bienstman, P.; Baets, R. *Opt. Lett.* **2004**, *29*, 2749–2751.
- (40) Freitag, M.; Low, T.; Xia, F. N.; Avouris, P. *Nat. Photonics* **2012**, *7*, 53–59.
- (41) Massicotte, M.; Schmidt, P.; Vialla, F.; Schädler, K. G.; Reserbat-Plantey, A.; Watanabe, K.; Taniguchi, T.; Tielrooij, K. J.; Koppens, F. H. L. *Nat. Nanotechnol.* **2015**, *11*, 42–46.
- (42) Lopez-Sanchez, O.; Lembke, D.; Kayci, M.; Radenovic, A.; Kis, A. *Nat. Nanotechnol.* **2013**, *8*, 497–501.
- (43) Furchi, M. M.; Polyushkin, D. K.; Pospischil, A.; Mueller, T. *Nano Lett.* **2014**, *14*, 6165–6170.
- (44) Haratipour, N.; Koester, S. J. *IEEE Electron Device Lett.* **2016**, *37*, 103–106.
- (45) Liu, H.; Neal, A. T.; Zhu, Z.; Luo, Z.; Xu, X.; Tománek, D.; Ye, P. D. *ACS Nano* **2014**, *8*, 4033–4041.
- (46) Saleh, B. E. A.; Teich, M. C. *Fundamentals of Photonics*; Wiley Series in Pure and Applied Optics; John Wiley & Sons, Inc.: New York, 1991.
- (47) Qiao, J.; Kong, X.; Hu, Z.-X.; Yang, F.; Ji, W. *Nat. Commun.* **2014**, *5*, 4475.
- (48) Buscema, M.; Groenendijk, D. J.; Blanter, S. I.; Steele, G. A.; Van Der Zant, H. S. J.; Castellanos-Gomez, A. *Nano Lett.* **2014**, *14*, 3347–3352.
- (49) Ye, L.; Li, H.; Chen, Z.; Xu, J. *ACS Photonics* **2016**, *3*, 692–699.
- (50) Li, L.; Engel, M.; Farmer, D. B.; Han, S. J.; Wong, H. S. P. *ACS Nano* **2016**, *10*, 4672–4677.
- (51) Long, G.; Maryenko, D.; Shen, J.; Xu, S.; Hou, J.; Wu, Z.; Wong, W. K.; Han, T.; Lin, J.; Cai, Y.; Lortz, R.; Wang, N. *Nano Lett.* **2016**, *16*, 7768–7773.
- (52) Wang, L.; Meric, I.; Huang, P. Y.; Gao, Q.; Gao, Y.; Tran, H.; Taniguchi, T.; Watanabe, K.; Campos, L. M.; Muller, D. A.; Guo, J.; Kim, P.; Hone, J.; Shepard, K. L.; Dean, C. R. *Science* **2013**, *342*, 614–617.
- (53) Barik, A.; Chen, X.; Oh, S.-H. *Nano Lett.* **2016**, *16*, 6317–6324.
- (54) Melikyan, A.; Alloatti, L.; Muslija, A.; Hillerkuss, D.; Schindler, P. C.; Li, J.; Palmer, R.; Korn, D.; Muehlbrandt, S.; Van Thourhout, D.; Chen, B.; Dinu, R.; Sommer, M.; Koos, C.; Kohl, M.; Freude, W.; Leuthold, J. *Nat. Photonics* **2014**, *8*, 229–233.
- (55) Youngblood, N.; Peng, R.; Nemilentsau, A.; Low, T.; Li, M. *ACS Photonics* **2016**, DOI: 10.1021/acsphotonics.6b00639.
- (56) Fiori, G.; Bonaccorso, F.; Iannaccone, G.; Palacios, T.; Neumaier, D.; Seabaugh, A.; Banerjee, S. K.; Colombo, L. *Nat. Nanotechnol.* **2014**, *9*, 768–779.
- (57) Willner, A. E.; Khaleghi, S.; Chitgarha, M. R.; Yilmaz, O. F. *J. Lightwave Technol.* **2014**, *32*, 660–680.